Journal of Materials Chemistry B

Accepted Manuscript

ROYAL SOCIETY OF CHEMISTRY

www.rsc.org/materialsB

Journal Name

RSCPublishing

COMMUNICATION

Tailoring Two-dimensional Graphene Oxide Surface: Dual T_1 and T_2 MRI Contrast Agent Materials

Cite this: DOI: 10.1039/x0xx00000x

Erwin Peng,‡[a] Fenghe Wang,‡[a] Suhui Tan,[a] Bingwen Zheng,[b] Sam Fong Yau Li[b,c] and Jun Min Xue*[a]

Received 00th January 2015,
Accepted 00th January 2015

DOI: 10.1039/x0xx00000x

www.rsc.org/

A generalized strategy for developing hybrid two-dimensional nanostructured dual T_1-T_2 MRI contrast agent (CA), by co-loading graphene oxide with both Mn-doped Fe_3O_4 (T_2 agent) and MnO (T_1 agent) magnetic nanoparticles, is reported. Typical T_1/T_2 signal quenching, due to magnetic coupling, was not observed because of the fair T_1 CA separation distance from the T_2 CA on the graphene oxide. The resultant two-dimensional nanostructured MRI CA complements the existing dual T_1-T_2 MRI CA libraries.

As one of the most powerful imaging platforms, magnetic resonance imaging (MRI) has become inseparable from the clinical imaging and medical diagnosis, especially for the soft tissues and organs visualization. Since MRI depends heavily on spatially localized magnetic nuclei within the human body to generate its basic contrast, the localized difference in the water proton intrinsic relaxation times becomes very critical. To considerably enhance the water protons' magnetic relaxation rate and thus improving the natural contrast of the imaging target and detection capabilities, exogenous contrast agent (CA) is purposely introduced. Depending on the water protons' relaxation mechanisms, MRI CAs can be divided into: (i) T_1 CAs that accelerate water protons' spin-lattice relaxation and (ii) T_2 CAs that accelerate water protons' spin-spin relaxation[1]. In the past decade, magnetic nanoparticles (MNPs) have been emerging as promising candidates for single-mode MRI CAs [1-2]. However, despite the prevailing contrast mechanism, single-mode MRI CA has its associated drawbacks that may put a limit on its extensive MRI clinical application. For instance, the induced magnetic susceptibility artifacts and the negative contrasting effects of the T_2 CA materials (*e.g.* superparamagnetic Fe_3O_4) may complicate the MRI images analysis[3]. Meanwhile, T_1 CA materials may provide excellent positive contrasting effect, at the expense of the required high concentration of toxic T_1 CA materials.

More recently, the development of dual-mode MRI contrast agent (or DMCA) that synergistically combined both T_1- and T_2-weighted imaging benefits, have gained significant research interest[4]. Currently, there are two possible strategies for fabricating DMCA (i) use of a single material that is capable of elucidating both T_1 and T_2 contrasting effect or (ii) combinatorial assembly of at least two MRI CA materials into one single nanostructure. The first strategy can be realized in zero-dimensional (0-D) nanostructures (*e.g.* single MNPs), while the latter can only be achieved in the nanostructures with higher-dimensionality (see **Scheme 1a**).

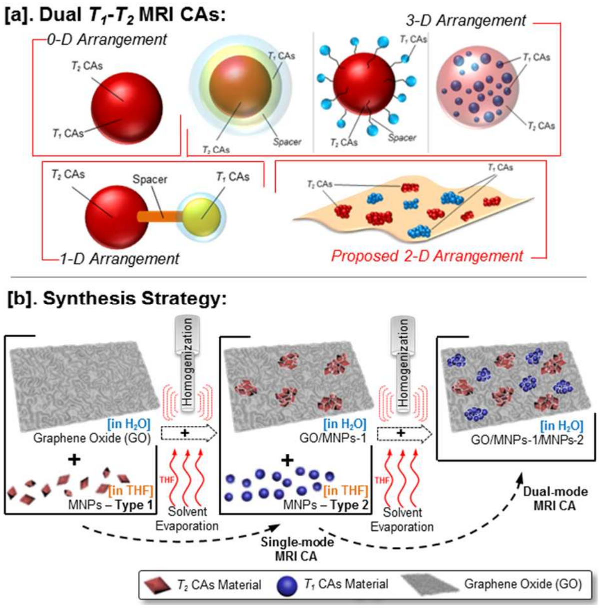

Scheme 1. (Top) Illustrations of various T_1-T_2 MRI contrast agent (DMCA) designs. (Bottom) Proposed strategy to fabricate DMCA based on the assembly of T_1 and T_2 nanoparticulate CAs on two-dimensional GO surface.

The simplest 0-D DMCA design involved the use of single-phase MNPs that were capable of concurrently enhancing both MRI T_1- and T_2-weighted imaging. These included ultra-small Fe_3O_4 MNPs[5], metal-doped Fe_3O_4 MNPs[6] as well as FeCo MNPs[7]. Due to the need to balance the relaxometric properties, 0-D DMCA often suffered from significantly low contrasting effect. To resolve this, T_1 and T_2 CA materials can be assembled into a more complex DMCA. One example was the direct conjugation of T_1 CA material (*e.g.* Gd- or Mn-based chelates) onto the of T_2 CA MNPs surface to form threedimensional (3-D) core-shell structure. These included Gd-labelled Fe_3O_4 MNPs[8], Gd-labelled $NaDyF_4$ MNPs[9] as well as $NaDyF_4$:Yb^{3+}/ $NaGdF_4$:Yb^{3+},Er^{3+} MNPs[10]. Such integration into single magnetic nanostructure often resulted in perturbation of T_1 CA by the T_2 CA local magnetic field inhomogeneities in the form of strong magnetic coupling; a phenomenon that was commonly regarded as magnetic quenching effect. Thus, the on-going DMCA studies emphasized on the importance of the optimized separation distance between T_1 and T_2 CA materials within a single nanostructure to achieve both high T_1 and T_2 contrasting effects. To realize this, several other unique architectures have been reported to promote magnetic decoupling and thus to reduce magnetic quenching effect. For instance, improved 3-D core-shell structure by introducing a non-magnetic silica spacer to distance the T_1 and T_2 CA materials [3b, 11] as well as seed-mediated synthesis to form one-dimensional (1-D) Fe_3O_4/Pt/Au@Gd-DOTA nanotrimers[12]. In a more extreme case, complex 3-D structure such as Gd-embedded Fe_3O_4 MNPs [13] or Eu-engineered iron oxide nanocubes [14] have also been reported previously in order to allow the T_1 CA material to exhibit similar parallel spin direction to the T_2 CA local magnetic field direction.

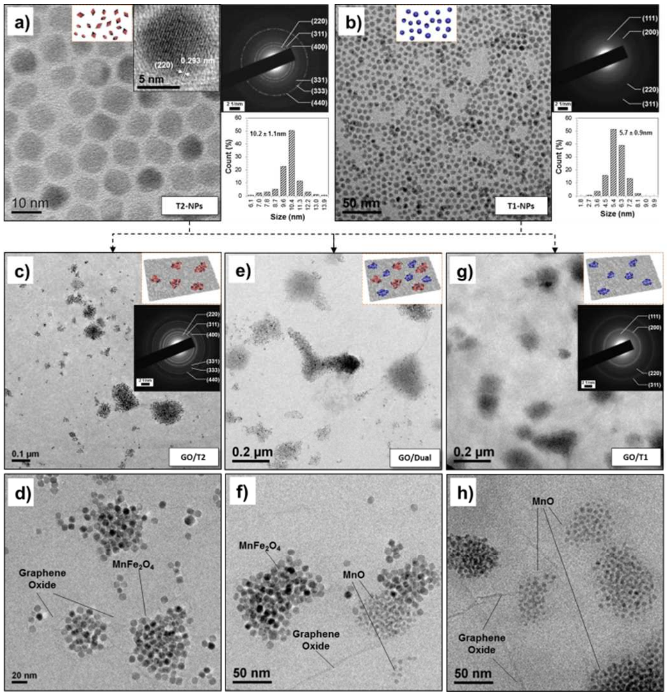

Fig. 1 [Top] TEM images of hydrophobic: (a) Mn-doped Fe_3O_4 (T_2-NPs) and (b) MnO (T_1-NPs) nanoparticles in $CHCl_3$ (clockwise: SAED patterns and TEM size distribution). [Bottom] TEM images of hydrophilic: (c,d) GO/T_2, (e,f) GO/Dual and (g,h) GO/T_1 magnetic nanocomposites (insets: SAED patterns).

Despite the numerous attempts to integrate T_1 and T_2 CA materials within a single nanostructure, it remains a great challenge to develop a facile method to synthesize DMCA with optimized T_1 and T_2 CAs separation distance. Herein, a new DMCA is proposed by co-loading T_1 and T_2 CAs onto graphene oxide (GO) sheets (**Scheme 1b**), tapping on the need to water-solubilize hydrophobic MNPs for biomedical applications.[15] (see ESI section S1 for detailed synthesis procedures)

T_2 and T_1 CA nanoparticles were prepared through the thermal decomposition of metal-organic precursors in non-polar solvent,[16] namely Mn-doped Fe_3O_4 (denoted as ***T_2*-NPs**) and MnO (denoted as ***T_1*-NPs**) MNPs. The TEM images of the MNPs dispersed in $CHCl_3$, given in **Fig. 1a,b**, indicated the successful formation of faceted T_2-NPs and spherical T_1-NPs. The average TEM sizes of the T_2-NPs and T_1-NPs were 10.2 ± 1.1 and 5.7 ± 0.9 nm, respectively. Due to the need of oleic acid capping agent to ensure the formation of high quality and monodisperse MNPs during the synthesis process, the as-synthesized MNPs were hydrophobic in nature and only dispersible in non-polar organic solvent. Post-synthetic water solubilisation process was essentially required to render these MNPs useful for biomedical application. To facilitate this, T_2-NPs and T_1-NPs were individually loaded onto hydrophilic GO sheets to form hydrophilic GO/T_2 and GO/T_1 nanocomposites. When both T_2-NPs and T_1-NPs were simultaneously loaded onto GO sheets using the proposed method, hybrid GO/Dual nanocomposites were formed. The TEM images (**Fig. 1c,d** and **Fig. 1g,h**) of the resultant GO/T_2 and GO/T_1 nanocomposites suggested the successful formation of two-dimensional nanostructures whereby the respective hydrophobic MNPs were decorated at the GO surface. Meanwhile, the TEM images (**Fig. 1e,f**) of GO/Dual nanocomposites confirmed the co-loading of both T_1-NPs and T_2-NPs at the GO sheets. The hydrophobic MNPs were preferentially aggregated and decorated at the hydrophobic segment of GO sheets' basal plane due to hydrophobic-hydrophobic interaction[17]. In addition to this, clear separation distance of more than 20 nm between T_1-NPs and T_2-NPs along the GO surface, which indicated the hydrophilic region of GO sheets, was also observed from the low magnification GO/Dual TEM image (see ESI; **Fig. S1**). By using a simple strategy, the separation distance between the hydrophobic MNPs clusters also can be tuned by varying the MNPs/GO mass ratio (see ESI; section S2, Fig. S2).

The crystalline phases of the hydrophobic MNPs and the hydrophilic GO/MNPs nanocomposites were investigated using x-ray diffraction (XRD). Based on the XRD patterns (**Fig. 2a**), the crystal structure of the T_2-NPs before and after loading remained unchanged with all the present characteristic peaks (at 2θ of 29.9°, 34.9°, 42.6°, 56.9° and 62.6°) indexed to the standard reflection pattern ((220), (311), (400), (333) and (440) planes, respectively) of cubic crystalline $MnFe_2O_4$ (Jacobsite; JCPDS #74-2403). The lattice fringes in the HRTEM of the T_2-NPs (inset of Fig. 2a) demonstrated that the NPs were highly crystallined with lattice spacing of 0.293 nm; which agreed well with the *d*-spacing of (220). The average crystallite size of T_2-NPs, calculated from Scherrer equation based on the most intense (311) XRD peak FWHM, was 9.78 nm which was in good agreement with its average TEM size. The selected area electron diffraction (SAED) patterns of T_2-NPs and GO/T_2 were also consistent with the characteristic Jacobsite phase. Meanwhile, all the present characteristic peaks (at 2θ of 35.1°, 41.8° and 59.1°) from T_1-NPs XRD patterns were indexed to the standard reflection pattern ((111), (200) and (220) planes, respectively) of cubic MnO (JCPDS #07-0230). Severe peak broadening was observed for T_1-NPs due to the nano-crystallite size effect. After loading of T_1-NPs onto GO sheets, no meaningful characteristic peaks were observed in the XRD pattern. Nevertheless, the SAED patterns of T_1-NPs and GO/T_1 were consistent with the standard MnO reflection pattern which indicated the successful loading of T_1-NPs into GO sheets.

XPS was conducted on T_1-NPs, GO as well as GO/T_1, GO/T_2 and GO/Dual nanocomposites. **Fig. 2b** summarized the wide-scan XPS survey spectra. The binding energy of the peaks has been calibrated to the C 1s sp^2 hybridized carbon peak at 284.6 eV. All the peaks could be assigned to the electronic transitions in Fe, Mn, O and C with the presence of Mn element for T_1-NPs, GO/T_1 and GO/Dual samples. From the XPS spectrum of C 1s (**Fig. 2c**), the presence of strong distinct peak of C–C bond at 284.6 eV with negligible C–O and C=O bonds at 286.6 eV and 288.4 eV respectively indicated the presence oleic acid coating within T1-NPs sample. For GO, GO/T_1, GO/T_2 and GO/Dual samples, the presence of strong and distinct peaks of C–O and C=O bonds at 286.6 eV and 288.4 eV respectively indicated the abundance of hydrophilic oxygen-containing functional groups that helped to stabilize the nanocomposites in aqueous solvent. Since MnO (Mn^{2+}) was favoured for MRI T_1 application due to the presence of abundant unpaired electrons than any other valence state of Mn ions, the successful formation of MnO phase was very critical. To further confirm the formation of MnO phase, the Mn oxidation states were determined from the XPS analysis. From the XPS spectrum of Mn 2p (**Fig. 2d**), the binding energy of Mn $2p_{3/2}$ peaks at 641.4 eV corresponded to the presence of Mn^{2+}. A slight appearance of Mn 2p satellite in the GO/T_1 and GO/Dual spectrum also indicated the presence Mn^{2+} oxidation state.

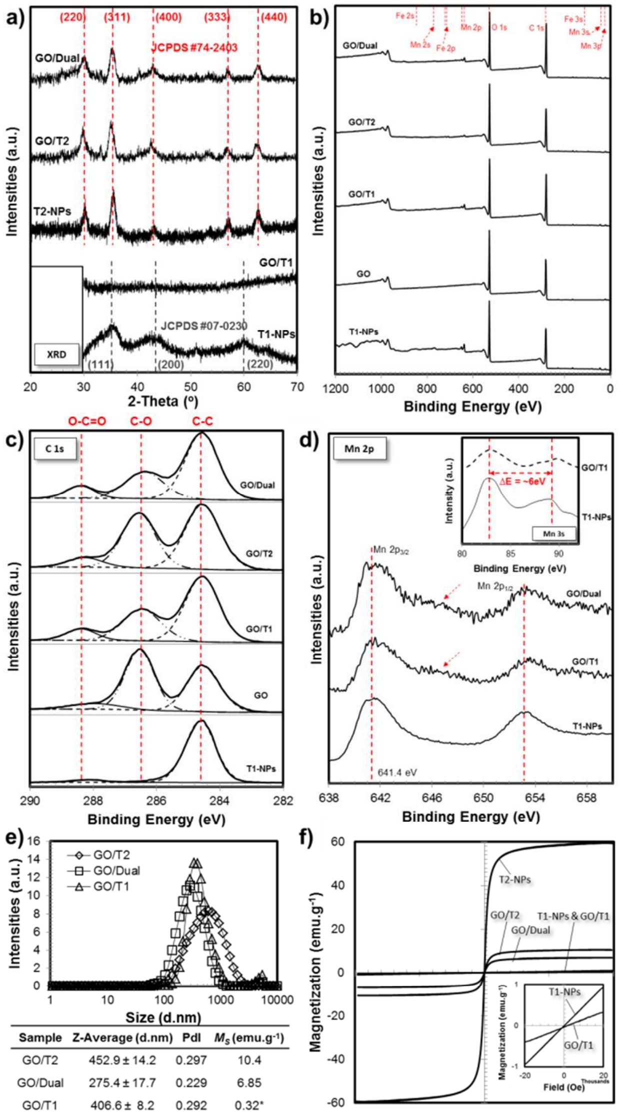

Sample	Z-Average (d.nm)	PdI	M_S (emu.g^{-1})
GO/T2	452.9 ± 14.2	0.297	10.4
GO/Dual	275.4 ± 17.7	0.229	6.85
GO/T1	406.6 ± 8.2	0.292	0.32*

* Magnetization at 20 kG

Fig. 2 (a) XRD patterns of hydrophobic T_1-NPs and T_2-NPs as well as hydrophilic GO/T_1, GO/T_2 and GO/Dual nanocomposites. (b) Wide-scan XPS spectra and (c) C 1s XPS spectra of T1-NPs, GO, GO/T_1, GO/T_2 and GO/Dual samples. (d) Mn 2p XPS spectra (inset: XPS spectrum of Mn 3s) of T_1-NPs, GO/T_1 and GO/Dual samples. (e) Hydrodynamic size distributions of various hydrophilic samples in water (25°C). (f) Hysteresis loops of hydrophobic T_1-NPs and T_2-NPs as well as hydrophilic nanocomposites (GO/T_2, GO/T_1 and GO/Dual), at 25°C.

In addition to this, the magnitude of the Mn 3s doublets splitting at approximately ΔE ~6eV (inset of Fig. 2d) was in a good agreement with the relative value of Mn^{2+} valence state. Both results indicated the oxidation state of Mn^{2+} that corresponded to the successful formation of MnO T_1-NPs and the presence of T_1-NPs in GO/T_1 and GO/Dual nanocomposites[18]. From the DLS size distributions (**Fig. 2e**), the hydrodynamic size (d_h) of GO/T_2, GO/Dual and GO/T_1 nanocomposites were 452.9 ± 14.2 nm, 275.4 ± 17.7 nm and 406.6 ± 8.2 nm, respectively. The d_h of GO/Dual was the lowest as compared to GO/T_1 and GO/T_2 nanocomposites. This was due to the incorporation of additional probe-sonication process that helped to break-up the GO sheets into much smaller pieces. The magnetic properties of both hydrophobic and hydrophilic samples were characterized by VSM. From the magnetic hysteresis loop profiles (**Fig. 2f**), T_2-NPs as well as GO/T_2 and GO/Dual exhibited superparamagnetism behaviour with saturation magnetization of 59.28 emu.g^{-1}, 10.4 emu.g^{-1} and 6.85 emu.g^{-1} respectively (at 20 kOe and 25°C). Meanwhile, T_1-NPs and hydrophilic GO/T_1 exhibited paramagnetic behaviours with mass magnetization of 0.94 emu.g^{-1} and 0.32 emu.g^{-1} (inset of **Fig. 2f**).

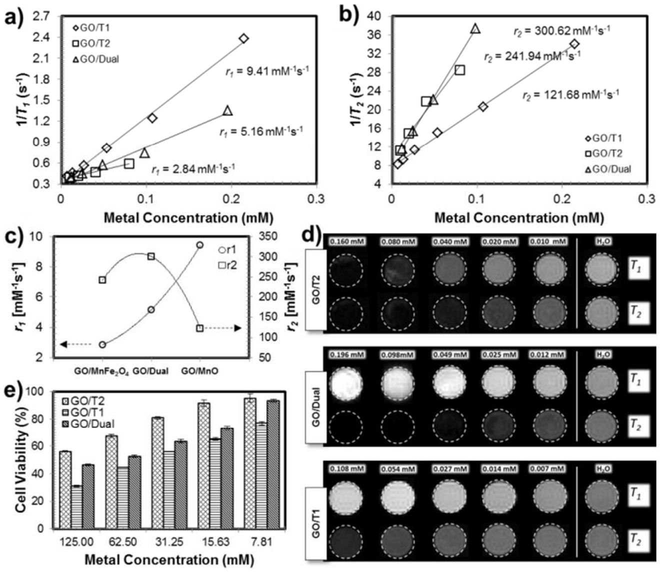

Fig. 3 (a) 1/T_1 and (b) 1/T_2 relaxation rates of hydrophilic GO/T_2, GO/Dual and GO/T_1 nanocomposites at different metal concentrations. (c) MR relaxivities summary and (d) concentration-dependent T_1- and T_2-weighted images of GO/T_2, GO/Dual and GO/T_1 nanocomposites. (e) In-vitro cell cytotoxicity of breast cancer cells (MCF-7) incubated with GO/T_2, GO/Dual and GO/T_1 nanocomposites at various metal concentrations.

The MR relaxivity measurements were performed for GO/T_2, GO/Dual and GO/T_1 using 7T MRI scanner. From the plot of T_1 and T_2 relaxation rates against various metal concentration (**Fig. 3a,b**), the r_1 values were 2.84 mM [Mn+Fe]$^{-1}$s^{-1}, 5.16 mM [Mn+Fe]$^{-1}$s^{-1} and 9.41 mM [Mn]$^{-1}$s^{-1} for GO/T_2, GO/Dual and GO/T_1 samples respectively. Meanwhile the r_2 values were 241.94 mM [Mn+Fe]$^{-1}$s^{-1}, 300.62 mM [Mn+Fe]$^{-1}$s^{-1} and 121.68 mM [Mn]$^{-1}$s^{-1} for GO/T_2, GO/Dual and GO/T_1 samples respectively. From the summary (**Fig. 3c**), r_1 value increased with the T_1-NPs loading while the r_2 value was enhanced with the combinatorial loading of both T_1-NPs and T_2-NPs. Finally, from the acquired T_1- and T_2-weighted images shown in **Fig. 3d**, it was clearly observed that both GO/T_2 and GO/T_1 exhibited their respective contrast enhancement effect: GO/T_2 shortened the transverse relaxation time, while GO/T_1 shortened the longitudinal relaxation time. When both T_1-NPs and T_2-NPs were co-loaded together, the shortening of both transverse and longitudinal relaxation times was observed. Moreover, if the r_1 value of GO/Dual was expressed in terms of the contributing Mn ion concentration only, the r_1 value of GO/Dual was 10.56 mM [Mn]$^{-1}$s^{-1} which was significantly comparable with the r_1 value of GO/T1.

Based on this comparison, the simultaneous presence of both T_1 CA and T_2 CA materials within GO/Dual nanocomposites did not annihilate the original individual MRI relaxometric properties. This can be attributed to the notable separation distance between T_1 CA and T_2 CA at GO sheet surface[11a]. In addition to this, , GO sheets surface was not covered by any undesirable molecules that might impair water diffusion and accessibility towards MNPs, except for the original MNPs oleic acid coating. Therefore, the 2-D assembly of both T_1-NPs and T_2-NPs on GO sheets also benefited from the improved water permeation and diffusivity of the GO host that promoted higher relaxivity rates[19].

Besides the MRI relaxometric properties, the cell viabilities of GO/T_2, GO/T_1 and GO/Dual samples were also determined after 24 hours incubation of MCF-7 breast cancer cells with respective samples. From the cell cytotoxicity assessment on MCF-7 cells (**Fig. 3e**) using CCK-8 assay, GO/T_1 that comprised of MnO MNPs exhibited lower viability as compared to GO/T_2 or GO/Dual. In general, the cell viability increased in the order of GO/T_1 < GO/Dual < GO/T_2. The high cellular cytotoxicity behaviour, especially for GO/T_1 with increasing MNPs loading, was expected due to the presence of hydrophobic oleic-acid coated MNPs on the surface of the GO sheets and the absence of any additional proper hydrophilic surface coating. The decreasing cell viability trend can therefore be ascribed to the presence of bare oleic-acid coated MNPs on GO surface that interacted directly with the surrounding environment[20]. To prevent this, additional surface modification, inclusive of non-covalent conjugation with Pluronic F127 block copolymers[21] or covalent conjugation with amine-bearing PEG functional group[22] can be imparted in future. Several preliminary results, inclusive of (i) the strategy on how to tune and control the hydrodynamic size of the nanocomposites, (ii) the formation of PEGylated hydrophilic magnetic nanocomposites and their MR relaxometric properties as well as (iii) the colloidal stability testing of GO/Dual nanocomposites, were summarized in the ESI; section S3 and S4.

Conclusions

In summary, a generalized simple protocol to fabricate two-dimensional dual T_1-T_2 MRI CAs has been presented. As a proof of concept, hydrophobic Mn-doped Fe_3O_4 and MnO MNPs were simultaneously water-solubilized and decorated onto GO sheets. Both MR relaxivity measurement and *in-vitro* cellular cytotoxicity assay have been performed. The resultant hydrophilic nanocomposites did not exhibit notable magnetic quenching effect due to the fair separation distance between T_1 CA and T_2 CA. Because of this, the resultant hydrophilic nanocomposites was able to induce both positive and negative contrasting effect. Such platform can be potentially extended to other magnetic or inorganic nanoparticles for multifunctional nanocomposites development.

Notes and references

Xue Jun Min and Erwin Peng would like to acknowledge the funding support by Singapore MOE Grant WBS R-284-000-102-112. Erwin Peng and Fenghe Wang contributed equally to this work.

Notes and references

[a] Department of Materials Science and Engineering.
Faculty of Engineering, National University of Singapore.
9 Engineering Drive 1, Singapore 117576.
Fax : +65 6776-3604; Tel : +65 6516-4655.
[b] Department of Chemistry. National University of Singapore.
3 Science Drive 3, Singapore 117543.
[c] NUS Environment Research Institute (NERI). Department of Chemistry.
3 Science Drive 3, Singapore 117573.

* Corresponding Authors:
Email: mseer@nus.edu.sg / msexuejm@nus.edu.sg

1 H. B. Na, I. C. Song and T. Hyeon, *Advanced Materials*, 2009, **21**, 2133.
2 F. Hu and Y. S. Zhao, *Nanoscale*, 2012, **4**, 6235.
3(a) J. W. M. Bulte and D. L. Kraitchman, *NMR in Biomedicine*, 2004, **17**, 484; (b) T.-H. Shin, J.-s. Choi, S. Yun, I.-S. Kim, H.-T. Song, Y. Kim, K. I. Park and J. Cheon, *ACS Nano*, 2014, **8**, 3393.
4(a) T.-H. Shin, Y. Choi, S. Kim and J. Cheon, *Chemical Society Reviews*, 2015; (b) E. Peng, F. Wang and J. M. Xue, *Journal of Materials Chemistry B*, 2015, **3**, 2241.
5(a) B. H. Kim, N. Lee, H. Kim, K. An, Y. I. Park, Y. Choi, K. Shin, Y. Lee, S. G. Kwon, H. B. Na, J.-G. Park, T.-Y. Ahn, Y.-W. Kim, W. K. Moon, S. H. Choi and T. Hyeon, *Journal of the American Chemical Society*, 2011, **133**, 12624; (b) Y. Tian, B. Yu, X. Li and K. Li, *Journal of Materials Chemistry*, 2011, **21**, 2476; (c) G. Wang, X. Zhang, A. Skallberg, Y. Liu, Z. Hu, X. Mei and K. Uvdal, *Nanoscale*, 2014, **6**, 2953; (d) H. Fengqin, J. Qiaojuan, L. Yilin and G. Mingyuan, *Nanotechnology*, 2011, **22**, 245604.
6(a) G. Huang, H. Li, J. Chen, Z. Zhao, L. Yang, X. Chi, Z. Chen, X. Wang and J. Gao, *Nanoscale*, 2014, **6**, 10404; (b) J. Wan, X. Jiang, H. Li and K. Chen, *Journal of Materials Chemistry*, 2012, **22**, 13500; (c) L. Wang, Q. Wu, S. Tang, J. Zeng, R. Qiao, P. Zhao, Y. Zhang, F. Hu and M. Gao, *RSC Advances*, 2013, **3**, 23454.
7 W. S. Seo, J. H. Lee, X. Sun, Y. Suzuki, D. Mann, Z. Liu, M. Terashima, P. C. Yang, M. V. McConnell, D. G. Nishimura and H. Dai, *Nat Mater*, 2006, **5**, 971.
8(a) K. H. Bae, Y. B. Kim, Y. Lee, J. Hwang, H. Park and T. G. Park, *Bioconjugate Chemistry*, 2010, **21**, 505; (b) Z. Wang, J. Liu, T. Li, J. Liu and B. Wang, *Journal of Materials Chemistry B*, 2014, **2**, 4748; (c) A. Szpak, S. Fiejdasz, W. Prendota, T. Strączek, C. Kapusta, J. Szmyd, M. Nowakowska and S. Zapotoczny, *J Nanopart Res*, 2014, **16**, 1.
9 J. Zhou, Z. Lu, G. Shan, S. Wang and Y. Liao, *Biomaterials*, 2014, **35**, 368.
10 Y. Zhang, G. K. Das, V. Vijayaragavan, Q. C. Xu, P. Padmanabhan, K. K. Bhakoo, S. Tamil Selvan and T. T. Y. Tan, *Nanoscale*, 2014, **6**, 12609.
11(a) J.-s. Choi, J.-H. Lee, T.-H. Shin, H.-T. Song, E. Y. Kim and J. Cheon, *Journal of the American Chemical Society*, 2010, **132**, 11015; (b) H. Yang, Y. Zhuang, Y. Sun, A. Dai, X. Shi, D. Wu, F. Li, H. Hu and S. Yang, *Biomaterials*, 2011, **32**, 4584.
12 K. Cheng, M. Yang, R. Zhang, C. Qin, X. Su and Z. Cheng, *ACS Nano*, 2014, **8**, 9884.
13(a) Z. Zhou, D. Huang, J. Bao, Q. Chen, G. Liu, Z. Chen, X. Chen and J. Gao, *Advanced Materials*, 2012, **24**, 6223; (b) Z. Zhou, L. Wang, X. Chi, J. Bao, L. Yang, W. Zhao, Z. Chen, X. Wang, X. Chen and J. Gao, *ACS Nano*, 2013, **7**, 3287; (c) X. Wang, Z. Zhou, Z. Wang, Y. Xue, Y. Zeng, J. Gao, L. Zhu, X. Zhang, G. Liu and X. Chen, *Nanoscale*, 2013, **5**, 8098.
14 L. Yang, Z. Zhou, H. Liu, C. Wu, H. Zhang, G. Huang, H. Ai and J. Gao, *Nanoscale*, 2015.
15 A. Quarta, A. Curcio, H. Kakwere and T. Pellegrino, *Nanoscale*, 2012, **4**, 3319.
16 L. Li, Y. Yang, J. Ding and J. Xue, *Chemistry of Materials*, 2010, **22**, 3183.
17 G. Huang, X. Zhu, H. Li, L. Wang, X. Chi, J. Chen, X. Wang, Z. Chen and J. Gao, *Nanoscale*, 2015, **7**, 2667.
18 J. Xiao, X. M. Tian, C. Yang, P. Liu, N. Q. Luo, Y. Liang, H. B. Li, D. H. Chen, C. X. Wang, L. Li and G. W. Yang, *Sci. Rep.*, 2013, **3**.
19(a) D. W. Boukhvalov, M. I. Katsnelson and Y.-W. Son, *Nano Letters*, 2013, **13**, 3930; (b) G. Gonçalves, M. Vila, I. Bdikin, A. de Andrés, N. Emami, R. A. S. Ferreira, L. D. Carlos, J. Grácio and P. A. A. P. Marques, *Sci. Rep.*, 2014, **4**.

20(a) S. Shukla, A. Jadaun, V. Arora, R. K. Sinha, N. Biyani and V. K. Jain, *Toxicology Reports*, 2015, **2**, 27; (b) W. Kai, X. Xiaojun, P. Ximing, H. Zhenqing and Z. Qiqing, *Nanoscale Research Letters*, 2011, **6**, 480.

21 B. J. Hong, O. C. Compton, Z. An, I. Eryazici and S. T. Nguyen, *ACS Nano*, 2011, **6**, 63.

22(a) Z. Liu, J. T. Robinson, X. Sun and H. Dai, *Journal of the American Chemical Society*, 2008, **130**, 10876; (b) E. Peng, E. S. G. Choo, P. Chandrasekharan, C.-T. Yang, J. Ding, K.-H. Chuang and J. M. Xue, *Small*, 2012, **8**, 3620; (c) H. Wen, C. Dong, H. Dong, A. Shen, W. Xia, X. Cai, Y. Song, X. Li, Y. Li and D. Shi, *Small*, 2012, **8**, 760.

Table of Content:

Image:

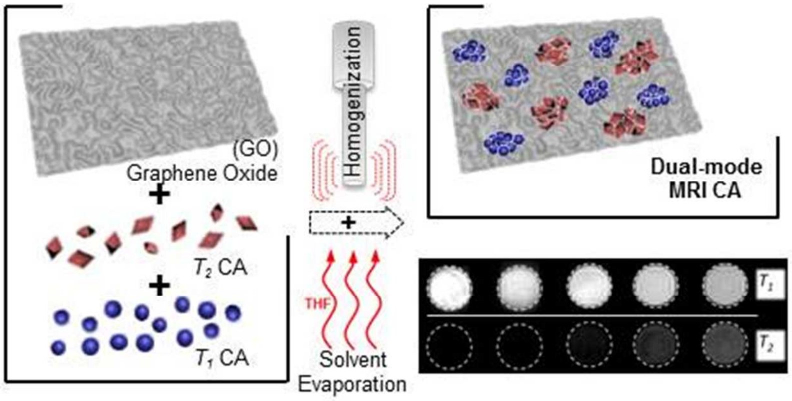

Description:

Water-soluble hybrid two-dimensional nanostructured dual T_1-T_2 MRI contrast agent with fair T_1 and T_2 nanoparticles separation distance and negligible T_1/T_2 signal quenching was developed.